Chapter 8

Significance of nanoparticle shape effect on MHD convective alumina-water nanofluid flow over a rotating rigid disk *

8.1 Introduction

This work aims in the numerical exploration of the hydromagnetic alumina–water nanofluid flow due to a rotating rigid disk. The nano fluid flow considering different nanoparticle shapes (namely sphere, platelet, cylinder, and brick) and the thermo-hydrodynamic slip constraints have been modeled utilizing the modified Buongiorno model. Modified Buongiorno model modifies the conventional two-phase Buongiorno model by additionally considering the volume fraction dependent nanoparticle properties. The present study has many applications in both engineering and industrial fields like spin coating, extrusion process, aerodynamics, etc. Von Kármán's similarity transformations are exercised in the transmutation of the mathematically modelled equations into a system of first-order ODE's and treated numerically using the generalized differential quadrature method. The consequence of effectual parameters on the physical quantities and the flow profiles is explained with the aid of graphs and tables.

8.2 Mathematical formulation

A steady hydromagnetic incompressible and axisymmetric alumina-water nanofluid flow due to a circular rigid disk placed at $z = 0$ has been considered (see Fig. 8.1). The flow is due to a constant rotation (Ω) of the disk which establishes a

*Published in: International Communications in Heat and Mass Transfer (Elsevier), 2022 (129); 105711

swirling flow in the neighbouring nanofluid layers. Let $(u,\ v,\ w)$ be the velocity components along $(r,\ \varphi,\ z)$ directions. Also, let $(T,\ T_W,\ T_\infty)$ be the nanofluid temperature, nanofluid temperature near the disk, and nanofluid temperature far from the disk, correspondingly and $(C,\ C_W,\ C_\infty)$ be the nanofluid concentration, nanofluid concentration near the disk, and nanofluid concentration far from the disk, respectively. An external magnetic field (of uniform intensity B_0) is applied along the axial direction. Using the two-phase modified Buongiorno nanofluid model (Yang et al., 2013), the governing equations take the form (see (Mustafa, 2017), (U. Khan, Bilal, Zaib, Makinde, & Wakif, 2022), (Mustafa et al., 2018)):

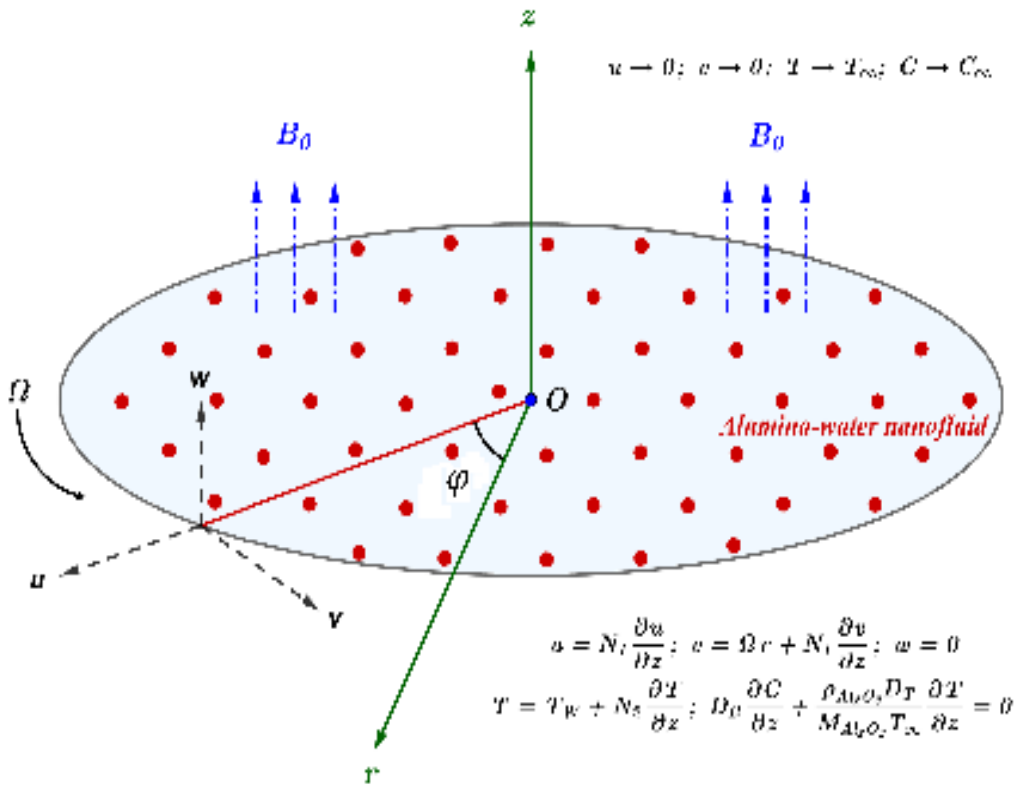

Figure 8.1: *Physical configuration*

$$\frac{\partial u}{\partial r}+\frac{u}{r}+\frac{\partial w}{\partial z}=0, \tag{8.2.1}$$

$$\rho_{nf}\left(u\frac{\partial u}{\partial r}-\frac{v^2}{r}+w\frac{\partial u}{\partial z}\right)=-\frac{\partial p}{\partial r}+\mu_{nf}\left(\frac{\partial^2 u}{\partial r^2}+\frac{1}{r}\frac{\partial u}{\partial r}-\frac{u}{r^2}+\frac{\partial^2 u}{\partial z^2}\right)-\sigma_{nf}B_o^2 u, \tag{8.2.2}$$

$$\rho_{nf}\left(u\frac{\partial v}{\partial r}+\frac{uv}{r}+w\frac{\partial v}{\partial z}\right)=\mu_{nf}\left(\frac{\partial^2 v}{\partial r^2}+\frac{1}{r}\frac{\partial v}{\partial r}-\frac{v}{r^2}+\frac{\partial^2 v}{\partial z^2}\right)-\sigma_{nf}B_o^2 v, \tag{8.2.3}$$

$$\rho_{nf}\left(u\frac{\partial w}{\partial r}+w\frac{\partial w}{\partial z}\right)=-\frac{\partial p}{\partial z}+\mu_{nf}\left(\frac{\partial^2 w}{\partial r^2}+\frac{1}{r}\frac{\partial w}{\partial r}+\frac{\partial^2 w}{\partial z^2}\right), \tag{8.2.4}$$

$$\begin{gathered}\left(\rho C_p\right)_{nf}\left(u\tfrac{\partial T}{\partial r}+w\tfrac{\partial T}{\partial z}\right)=k_{nf}\left(\tfrac{\partial^2 T}{\partial r^2}+\tfrac{1}{r}\tfrac{\partial T}{\partial r}+\tfrac{\partial^2 T}{\partial z^2}\right)+\\ \left(\rho C_p\right)_p\left\{\tfrac{D_B M_{Al_2O_3}}{\rho_{Al_2O_3}}\left(\tfrac{\partial T}{\partial z}\tfrac{\partial C}{\partial z}+\tfrac{\partial T}{\partial r}\tfrac{\partial C}{\partial r}\right)+\tfrac{D_T}{T_\infty}\left[\left(\tfrac{\partial T}{\partial z}\right)^2+\left(\tfrac{\partial T}{\partial r}\right)^2\right]\right\}\end{gathered} \tag{8.2.5}$$

$$u\frac{\partial C}{\partial r}+w\frac{\partial C}{\partial z}=D_B\left(\frac{\partial^2 C}{\partial z^2}+\frac{1}{r}\frac{\partial C}{\partial r}+\frac{\partial^2 C}{\partial r^2}\right)+\frac{\rho_{Al_2O_3}D_T}{M_{Al_2O_3}T_\infty}\left(\frac{\partial^2 T}{\partial r^2}+\frac{1}{r}\frac{\partial T}{\partial r}+\frac{\partial^2 T}{\partial z^2}\right), \tag{8.2.6}$$

subject to the following boundary conditions

$$\left.\begin{gathered}u=N_1\tfrac{\partial u}{\partial z},\ v=r\Omega+N_1\tfrac{\partial v}{\partial z},w=0,\\ T=T_w+N_2\tfrac{\partial T}{\partial z},D_B\tfrac{\partial C}{\partial z}+\tfrac{\rho_{Al_2O_3}D_T}{M_{Al_2O_3}T_\infty}\tfrac{\partial T}{\partial z}=0\end{gathered}\right\}\ \text{at}\ \ z=0 \tag{8.2.7}$$

$$u\to 0\ ,\ v\to 0\ ,\ T\to T_\infty\ ,\ C\to C_\infty\ \ \text{as}\ \ z\to\infty \tag{8.2.8}$$

Physical quantities of interest are (see (Mustafa et al., 2018)):
Local Skin friction coefficient :

$$C_f=\frac{\sqrt{\tau_r^2+\tau_\varphi^2}}{\rho_f(r\Omega)^2}\ ;\tau_r=\mu_{nf}\left.\frac{\partial u}{\partial z}\right|_{z=0}\ \ \&\ \ \tau_\varphi=\mu_{nf}\left.\frac{\partial v}{\partial z}\right|_{z=0}. \tag{8.2.9}$$

Local Nusselt number:

$$Nu=\frac{rq_w}{k_f\left(T_W-T_\infty\right)}\ ;q_w=k_{nf}\left.\frac{\partial T}{\partial z}\right|_{z=0}. \tag{8.2.10}$$

Introducing the following similarity transformations (see (Mahanthesh, Lorenzini, Oudina, & Animasaun, 2020)) into equations (8.2.1) to (8.2.10)
$\zeta=z\sqrt{\frac{\Omega}{\nu_f}},\ u=\ \Omega r\ F\left(\zeta\right)\ ,$
$v=\ \Omega r\ G\left(\zeta\right)\ ,w=\sqrt{\nu_f\Omega}\ H\left(\zeta\right)\ ,p=p_\infty-2\Omega\ \mu_f\ P\left(\zeta\right)\ ,$
$T=T_\infty+\left(\mathrm{T}_w-T_\infty\right)\ \theta\left(\zeta\right)\ ,C=C_\infty+\left(C_W-C_\infty\right)\ \phi\left(\zeta\right)$
The reduced governing equations are given by:

$$2F+H_\zeta=0 \tag{8.2.11}$$

$$F_{\zeta\zeta}-\frac{A_3}{A_1}MF+\frac{A_2}{A_1}\left(G^2-F^2-F_\zeta H\right)=0 \tag{8.2.12}$$

$$G_{\zeta\zeta} - \frac{A_3}{A_1} MG - \frac{A_2}{A_1} \left(2FG + G_\zeta H\right) = 0 \tag{8.2.13}$$

$$\theta_{\zeta\zeta} + \frac{Pr}{A_4} \left(Nb\chi_\zeta \theta_\zeta + Nt\theta_\zeta^2 - A_5 H\theta_\zeta\right) = 0 \tag{8.2.14}$$

$$\phi_{\zeta\zeta} + \frac{Nt}{Nb}\theta_{\zeta\zeta} - ScH\phi_\zeta = 0 \tag{8.2.15}$$

with

$$\begin{gathered} F\left(0\right) = b_1\ F_\zeta\left(0\right)\ ,\ G\left(0\right) = 1 + b_1\ G_\zeta\left(0\right)\ ,\ H\left(0\right) = 0\ , \\ \theta\left(0\right) = 1 + \gamma\ \theta_\zeta\left(0\right)\ ,\ \chi_\zeta\left(0\right) + \tfrac{Nt}{Nb}\theta_\zeta\left(0\right) = 0\ ,\ F\left(\zeta \to \infty\right) \to 0, \\ G\left(\zeta \to \infty\right) \to 0\ ,\ \theta\left(\zeta \to \infty\right) \to 0\ ,\ \phi\left(\zeta \to \infty\right) \to 0\ . \end{gathered} \tag{8.2.16}$$

The physical quantities in their reduced form are:

$$C_{fr} = C_f\ Re^{1/2} = A_1\ \sqrt{F_\zeta^2\left(0\right) + G_\zeta^2\left(0\right)}\ . \tag{8.2.17}$$

$$Nu_r = Nu\ Re^{-1/2}\ = -A_4\ \theta_\zeta\left(0\right)\ . \tag{8.2.18}$$

where M (magnetic field parameter)$= \frac{\sigma_f B_0^2}{\rho_f \Omega}$, τ (effective heat capacity ratio)$= \frac{\left(\rho C_P\right)_p}{\left(\rho C_P\right)_f}$, Pr (Prandtl number)$= \frac{\left(\mu C_P\right)_f}{\kappa_f}$, Nt (thermophoresis parameter)$= \frac{\tau\ D_T(T_w - T_\infty)}{T_\infty \nu_f}$, Nb (Brownian motion parameter)$= \frac{\tau\ M_{Al_2O_3} D_B (C_w - C_\infty)}{\rho_{Al_2O_3} \nu_f}$, Sc (Schmidt number)$= \frac{\nu_f}{D_B}$, b_1 (hydrodynamic slip parameter)$= N_1 \left(\frac{\Omega}{\nu_f}\right)^{\frac{1}{2}}$, γ (thermal slip parameter)$= N_2 \left(\frac{\Omega}{\vartheta_f}\right)^{\frac{1}{2}}$, and Re (local Reynold's number)$= \frac{\Omega r^2}{\nu_f}$ are the nondimensional quantities. The nanofluid models, thermophysical properties and the nanoparticle shape characteristics are described in Tables 8.1, 8.2 and 8.3 respectively.

Table 8.1: *Effective nanofluid constants see (Timofeeva et al., 2009),(Mustafa et al., 2018),(Brinkman, 1952).*

Non-spherical Nanoparticles	Spherical Nanoparticles
$A_1 = \frac{\mu_{nf}}{\mu_f} = 1 + a_1\phi_{Al_2O_3} + a_2\phi_{Al_2O_3}^2$	$A_1 = \frac{\mu_{nf}}{\mu_f} = \frac{1}{\left(1-\phi_{Al_2O_3}\right)^{2.5}}$
$A_2 = \frac{\rho_{nf}}{\rho_f} = \left(1 - \phi_{Al_2O_3}\right) + \phi_{Al_2O_3}\left(\frac{\rho_{Al_2O_3}}{\rho_f}\right)$	
$A_3 = \frac{\sigma_{nf}}{\sigma_f} = 1 + \frac{3\left(\frac{\sigma_{Al_2O_3}}{\sigma_f} - 1\right)\phi_{Al_2O_3}}{\left(\frac{\sigma_{Al_2O_3}}{\sigma_f} + 2\right) - \left(\frac{\sigma_{Al_2O_3}}{\sigma_f} - 1\right)\phi_{Al_2O_3}}$	
$A_4 = \frac{k_{nf}}{k_f} = \frac{k_{Al_2O_3} + (\widetilde{n_s} - 1)k_f - (\widetilde{n_s} - 1)\varphi\left(k_f - k_{Al_2O_3}\right)}{k_{Al_2O_3} + (\widetilde{n_s} - 1)k_f + \phi_{Al_2O_3}\left(k_f - k_{Al_2O_3}\right)}$	
$A_5 = \frac{\left(\rho C_P\right)_{nf}}{\left(\rho C_P\right)_f} = \left(1 - \phi_{Al_2O_3}\right) + \phi_{Al_2O_3}\frac{\left(\rho C_p\right)_{Al_2O_3}}{\left(\rho C_p\right)_f}$	

Table 8.2: *Thermophysical Properties of water and Al_2O_3 (see (Wakif & Sehaqui, 2022)).*

Physical Properties	Water	Al_2O_3
$\rho\ (kg/m^3)$	997.1	3970
$k\ (W/m.K)$	0.613	40
$\sigma\ (S/m)$	0.05	10^{-10}
$C_P\ (J/kg.K)$	4179	765
$\mu\ (Pa.s)$	89 $\times 10^{-5}$	—

8.3 Numerical solution

Generalized differential quadrature method (GDQM) acts as a powerful numerical collocation method for tackling linear and nonlinear physical problems due to its high flexibility and higher accuracy levels. More description on the solving procedure for the proposed GDQM can be seen in (Thumma, Wakif, & Animasaun, 2020), (Nayak, Wakif, Animasaun, & Alaoui, 2020). Fig. 8.2 depicts a brief outline on the steps involved in adopted numerical procedure. The conversion of the infinite physical domain $[0, \infty]$ to the finite computational domain $[0, 1]$ is achieved with the aid of the following transformations:

$$\left.\begin{array}{c} \zeta = \zeta_\infty\ \eta \\ F(\zeta) = F(\zeta_\infty\ \eta) = \tilde{F}(\eta) \\ G(\zeta) = G(\zeta_\infty\ \eta) = \tilde{G}(\eta) \\ H(\zeta) = H(\zeta_\infty\ \eta) = \tilde{H}(\eta) \\ \theta(\zeta) = \theta(\zeta_\infty\ \eta) = \tilde{\theta}(\eta) \\ \phi(\zeta) = \phi(\zeta_\infty\ \eta) = \tilde{\phi}(\eta) \end{array}\right\} \tag{8.3.1}$$

where ζ_∞ is the appropriate asymptotical value taken by the boundary layer thickness.

The reduced ODE's, boundary conditions, and physical quantities are transformed (using equation (8.3.1)) into:

$$2\ \zeta_\infty\ \tilde{F} + \tilde{H}_\eta = 0 \tag{8.3.2}$$

$$\tilde{F}_{\eta\eta} - \frac{A_3}{A_1}\ \zeta_\infty^2\ M\ \tilde{F} + \frac{A_2}{A_1}\left(\ \zeta_\infty^2\ \tilde{G}^2 -\ \zeta_\infty^2\ \tilde{F}^2 -\ \zeta_\infty\ \tilde{F}_\eta\ \tilde{H}\right) = 0 \tag{8.3.3}$$

$$\tilde{G}_{\eta\eta} - \frac{A_3}{A_1}\ \zeta_\infty^2\ M\ \tilde{G} - \frac{A_2}{A_1}\left(2\ \zeta_\infty^2\ \tilde{F}\ \tilde{G} +\ \zeta_\infty\ \tilde{G}_\eta\ \tilde{H}\right) = 0 \tag{8.3.4}$$

Table 8.3: *Nanoparticle shape properties of Al_2O_3 (see (Timofeeva et al., 2009)).*

Characteristics of nanoparticles	Sphere	Platelet	Cylinder	Brick
a_1	——	37.1	13.5	1.9
a_2	——	612.6	904.4	471.4
Sphericity χ	1	0.52	0.62	0.81
Shape factor $\widetilde{n_s} = \frac{3}{\chi}$	3	5.7	4.9	3.7

$$\tilde{\theta}_{\eta\eta} + \frac{Pr}{A_4}\left(Nb\ \tilde{\theta}_\eta\ \tilde{\chi}_\eta + Nt\ \tilde{\theta}_\eta^2 - A_5\ \zeta_\infty\ \tilde{H}\ \tilde{\theta}_\eta\right) = 0 \tag{8.3.5}$$

$$\tilde{\phi}_{\eta\eta} + \frac{Nt}{Nb}\ \tilde{\theta}_{\eta\eta} - Sc\ \zeta_\infty\ \tilde{H}\ \tilde{\phi}_\eta = 0 \tag{8.3.6}$$

with

$$\left.\begin{array}{c} \tilde{F}(0) = \frac{b_1}{\zeta_\infty}\ \tilde{F}_\eta(0)\ ,\ \tilde{G}(0) = 1 + \frac{b_1}{\zeta_\infty}\ \tilde{G}_\eta(0)\ ,\ \tilde{H}(0) = 0\ , \\ \tilde{\theta}(0) = 1 + \frac{\gamma}{\zeta_\infty}\ \tilde{\theta}_\eta(0)\ ,\ \tilde{\phi}_\eta(0) + \frac{Nt}{Nb}\tilde{\theta}_\eta(0) = 0\ , \\ \tilde{F}(\eta \to 1) \to 0\ ,\ \tilde{G}(\eta \to 1) \to 0\ ,\ \tilde{\theta}(\eta \to 1) \to 0\ ,\ \tilde{\phi}(\eta \to 1) \to 0\ . \end{array}\right\} \tag{8.3.7}$$

$$Re^{1/2}C_{fr}\ = \frac{A_1}{\zeta_\infty}\ \sqrt{\tilde{F}_\eta^2(0) + \tilde{G}_\eta^2(0)} \tag{8.3.8}$$

$$Re^{-1/2}Nu_r = -\frac{A_4}{\zeta_\infty}\ \tilde{\theta}_\eta(0) \tag{8.3.9}$$

In order to achieve a higher level of accuracy, the transformed ODEs are spatially discretized utilizing the modified Gauss-Lobatto grid points $\left\{\eta_i \mid 0 \leq \eta_i\ \leq 1\quad \&\quad 1 \leq i \leq \tilde{N}\right\}$ given by

$$\eta_i = \frac{1}{2} - \frac{1}{2}cos\left(\frac{\pi(i-1)}{\tilde{N}-1}\right) \tag{8.3.10}$$

where $\tilde{N}$ is the total number of collocation points. The numerical discretization of the space derivative for a continuous function $T(\eta)$ at any collocation point η_i is given by

$$T^{(\tilde{n})}(\eta_i) = \sum_{j=1}^{\tilde{N}} d_{ij}^{(\tilde{n})}\ T_j \tag{8.3.11}$$

where $T_j = T(\eta_j)\quad \&\quad 1 \leq i,\ j \leq \tilde{N}$ are the weighting coefficients for the $\tilde{n}^{th}$-order derivative.

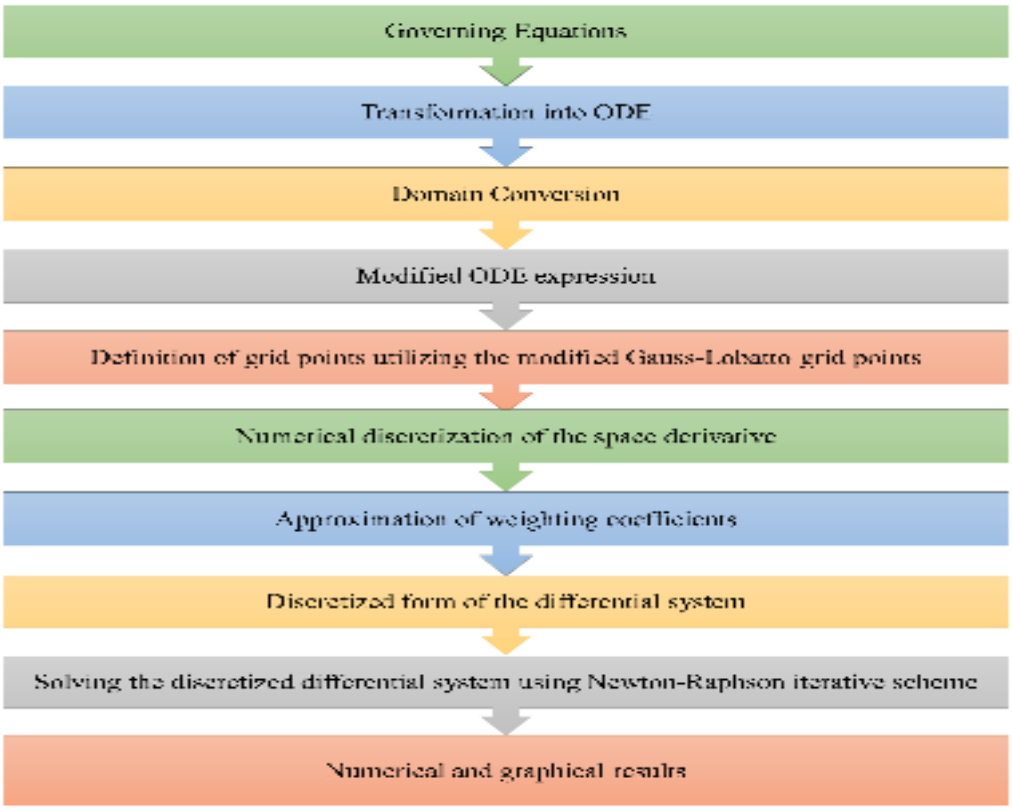

Figure 8.2: *Flowchart depicting the numerical scheme.*

According to (Shu, 2012) and (X. Wang, 2015), the coefficients $d_{ij}^{(\tilde{n})}$ are explicitly defined as:

$$\left.\begin{aligned} d_{ij}^{(1)} &= \frac{\prod_{k=1,k\neq i}^{\tilde{N}}(\eta_i-\eta_k)}{(\eta_i-\eta_j)\prod_{k=1,k\neq j}^{\tilde{N}}(\eta_j-\eta_k)} \quad for\ i\neq j,\ 1\leq i,\ j\leq \tilde{N}.\\ d_{ij}^{(1)} &= \sum_{k=1,k\neq i}^{\tilde{N}} d_{ik}^{(1)} \quad for\ i=j,\ 1\leq i,\ j\leq \tilde{N}.\\ d_{ij}^{(\tilde{n})} &= \tilde{n}\left[d_{ii}^{(\tilde{n}-1)}d_{ij}^{(1)} - \frac{d_{ij}^{(\tilde{n}-1)}}{\eta_i-\eta_j}\right] \quad for\ i\neq j,\ 1\leq i,\ j\leq \tilde{N} \quad \& \quad \tilde{n}\geq 2.\\ d_{ij}^{(\tilde{n})} &= -\sum_{k=1,\ k\neq i}^{\tilde{N}} d_{ik}^{(\tilde{n})} \quad for\ i=j,\ 1\leq i,\ j\leq \tilde{N} \quad \& \quad \tilde{n}\geq 2. \end{aligned}\right\} \tag{8.3.12}$$

Applying GDQM approximation to equations (8.3.2)-(8.3.7), the discretized nonlinear differential system is given by:

$$NDS:$$

$$\tilde{F}_i - \tfrac{b_1}{\zeta_\infty} \sum_{j=1}^{\tilde{N}} d_{ij}^{(1)}\ \tilde{F}_j = 0, \quad for\ i = 1,$$

$$\tfrac{A_2}{A_1}\left(\zeta_\infty^2\ \tilde{G}_i^2 - \ \zeta_\infty^2\ \tilde{F}_i^2 - \ \zeta_\infty \sum_{j=1}^{\tilde{N}} d_{ij}^{(1)}\ \tilde{H}_i\ \tilde{F}_j \right)$$

$$+\sum_{j=1}^{\tilde{N}} d_{ij}^{(2)}\ \tilde{F}_j - \tfrac{A_3}{A_1}\ \zeta_\infty^2\ M\ \tilde{F}_i = 0 \quad for \quad i = 2 \leq i \leq \tilde{N} - 1.$$

$$\tilde{F}_i = 0,\ for\ i = \tilde{N},.$$

$$\tilde{G}_i - \left(1 + \tfrac{b_1}{\zeta_\infty} \sum_{j=1}^{\tilde{N}} d_{ij}^{(1)}\ \tilde{G}_j \right) = 0,\ for\ i = 1,$$

$$\sum_{j=1}^{\tilde{N}} d_{ij}^{(2)}\ \tilde{G}_j - \tfrac{A_2}{A_1}\left(2\ \zeta_\infty^2\ \tilde{F}_i\ \tilde{G}_i + \ \zeta_\infty \sum_{j=1}^{\tilde{N}} d_{ij}^{(1)}\ \tilde{H}_i\ \tilde{G}_j \right)$$

$$-\tfrac{A_3}{A_1}\ \zeta_\infty^2\ M\ \tilde{G}_i = 0,\ for\ i = 2 \leq i \leq \tilde{N} - 1,$$

$$\tilde{G}_i = 0, \quad for\ i = \tilde{N},$$

$$\tilde{H}_i = 0, \quad for\ i = 1,$$

$$2\ \zeta_\infty\ \tilde{F}_i + \sum_{j=1}^{\tilde{N}} d_{ij}^{(1)}\ \tilde{H}_j = 0, \quad for\ i = 2 \leq i \leq \tilde{N} - 1,$$

$$\tilde{\theta}_i - \left(1 + \tfrac{\gamma}{\zeta_\infty} \sum_{j=1}^{\tilde{N}} d_{ij}^{(1)}\ \tilde{\theta}_j \right) = 0,\ for\ i = 1,$$

$$\tfrac{Pr}{A_4}\left(Nb \sum_{j=1}^{\tilde{N}} d_{ij}^{(1)}\ \tilde{\theta}_j \sum_{j=1}^{\tilde{N}} d_{ij}^{(1)}\ \tilde{\phi}_j + Nt \left(\sum_{j=1}^{\tilde{N}} d_{ij}^{(1)}\ \tilde{\theta}_j \right)^2 - A_5\ \zeta_\infty \ \sum_{j=1}^{\tilde{N}} d_{ij}^{(1)}\ \tilde{H}_i\ \tilde{\theta}_j \right)$$

$$+\sum_{j=1}^{\tilde{N}} d_{ij}^{(2)}\ \tilde{\theta}_j = 0, \quad for\ i = 2 \leq i \leq \tilde{N} - 1,$$

$$\tilde{\theta}_i = 0,\ for\ i = \tilde{N},$$

$$\sum_{j=1}^{\tilde{N}} d_{ij}^{(1)}\ \tilde{\phi}_j + \tfrac{Nt}{Nb} \sum_{j=1}^{\tilde{N}} d_{ij}^{(1)}\ \tilde{\theta}_j = 0,\ for\ i = 1,$$

$$\sum_{j=1}^{\tilde{N}} d_{ij}^{(2)}\ \tilde{\phi}_j + \tfrac{Nt}{Nb} \sum_{j=1}^{\tilde{N}} d_{ij}^{(2)}\ \tilde{\theta}_j - Sc\ \zeta_\infty \ \sum_{j=1}^{\tilde{N}} d_{ij}^{(1)}\ \tilde{H}_i\ \tilde{\phi}_j = 0,\ \text{for } i = 2 \leq i \leq \tilde{N} - 1,$$

$$\tilde{\phi}_i = 0\ for\ i = \tilde{N}.$$

The above non-linear algebraic system (NDS) is solved iteratively utilizing Newton-Raphson method and by taking $\left(\zeta_\infty\ , \tilde{N}\right) = (30, 100)$ as the best key values with an accuracy of 10^{-11}. After accurate generation of the discrete solutions $\left\{ \tilde{F}\left(\eta_i\right)\ ,\ \tilde{G}\left(\eta_i\right)\ ,\ \tilde{\theta}\left(\eta_i\right)\ ,\ \tilde{\phi}\left(\eta_i\right)\ \mid 1 \leq i \leq \tilde{N} \right\}$ locally, the flow profiles and the physical quantities can be deduced as:

$$F\left(\zeta_i\right) = \tilde{F}\left(\eta_i\right) \tag{8.3.13}$$

$$G\left(\zeta_i\right) = \tilde{G}\left(\eta_i\right), \tag{8.3.14}$$

$$H\left(\zeta_i\right) = \tilde{H}\left(\eta_i\right), \tag{8.3.15}$$

$$\theta\left(\zeta_i\right) = \tilde{\theta}\left(\eta_i\right) \tag{8.3.16}$$

$$\phi\left(\zeta_i\right) = \tilde{\phi}\left(\eta_i\right), \tag{8.3.17}$$

$$C_{fr} = \frac{A_1}{\zeta_\infty} \sqrt{\left(\sum_{j=1}^{\tilde{N}} d_{1j}^{(1)}\ \tilde{F}_j\right)^2 + \left(\sum_{j=1}^{\tilde{N}} d_{1j}^{(1)}\ \tilde{G}_j\right)^2} \tag{8.3.18}$$

$$Nu_r = -\frac{A_4}{\zeta_\infty} \sum_{j=1}^{\tilde{N}} d_{1j}^{(1)}\ \tilde{\theta}_j \tag{8.3.19}$$

The veracity of the code and the validation of the current problem have been adjudged through a restrictive comparison with already published works (see Tables 8.4 and 8.5).

Table 8.4: *Validation for regular fluids ($Pr = 6.2$, $\phi_{Al_2O_3} = 0$, $M = 0$, $b_1 = 0$, $\gamma = 0$, $\zeta_\infty = 30$, $\tilde{N} = 100$)*

Physical Quantities	(Turkyilmazoglu, 2014)	(J. A. Khan, Mustafa, Hayat, & Alsaedi, 2018)	Present Results
$F_\zeta(0)$	0.51023262	0.510232	0.510232619
$-G_\zeta(0)$	0.61592201	0.615923	0.615922014
$-H(\infty)$	0.88447411	0.88462	0.88447411
$-\theta_\zeta(0)$.	0.93387794	0.933877	0.93387794

Table 8.5: *Validation for nanofluids ($Pr = 7$, $A_1 = A_2 = A_3 = A_4 = A_5 = 1$, $Sc = 5$, $Nb = 0.5$, $Nt = 0.5$, $b_1 = 0$, $\gamma = 0$, $\zeta_\infty = 15$, $\tilde{N} = 100$)*

M	(J. A. Khan et al., 2018)		Present Results	
	$-\theta_\zeta(0)$	$\sqrt{F_\zeta^2(0) + G_\zeta^2(0)}$	$-\theta_\zeta(0)$	$\sqrt{F_\zeta^2(0) + G_\zeta^2(0)}$
0.5	———	0.93201894	0.642783196	0.932018932
1	0.50409254	1.1128862	0.504092494	1.112886149
1.5	———	1.2929102	0.392295982	1.292910169
2	———	1.4604084	0.306400265	1.460408379
2.5	———	1.6148965	0.242922257	1.614896532

8.4 Results and Discussion

The consequence of pertinent parameters over the radial velocity ($F(\zeta)$), azimuthal velocity ($G(\zeta)$), nanofluid temperature profile ($\theta(\zeta)$), and nanofluid concentration profiles ($\phi(\zeta)$) has been depicted through Figs. 8.3-8.23. The Prandtl number and infinity are chosen as 6.2 and 8, respectively. The thermophysical properties of water and alumina nanoparticles are identified in Table 8.2. The base values for the effectual parameters are fixed at $\phi_{Al_2O_3} = 0.02$, $M = 0.2$, $Sc = 5$, $Nb = 0.2$, $Nt = 0.1$, $b_1 = 0.25$, $\gamma = 0.25$. Further, the impact of nanoparticle shape factor on the physical quantities is elucidated in Tables 8.6 and 8.7.

Figs. 8.3 and 8.4 display the variation in $F(\zeta)$ and $G(\zeta)$ for differing values of $\phi_{Al_2O_3}$, respectively. Both $F(\zeta)$ and $G(\zeta)$ elevates with augmentation in $\phi_{Al_2O_3}$. The radial velocity profile attains the maximum value after travelling a distance from the disk and finally converges asymptotically whereas the azimuthal velocity profile achieves the highest magnitude near the disk and reduces subsequently. The elevation in $\theta(\zeta)$ due to an increment in $\phi_{Al_2O_3}$ is depicted in Fig. 8.5. This escalation in the nanofluid temperature is due to the enhanced thermal conductivity and also due to the increased frictional drag initiated by the hike in nanofluid viscosity.

The influence of M on the radial and azimuthal velocity profiles is shown in

Table 8.6: *Numerical estimation of Cf_r for various shapes of nanoparticles ($M = 0.2$, $Sc = 5$, $Nb = 0.2$, $Nt = 0.1$, $b_1 = 0.25$, $\gamma = 0.25$, $\zeta_\infty = 30$, $\tilde{N} = 100$)*

$\widetilde{n}_s$	Cf_r				Slope of $Cf_r = f(\widetilde{n}_s, \phi_{Al_2O_3})$
	$\phi_{Al_2O_3} = 0.01$	$\phi_{Al_2O_3} = 0.02$	$\phi_{Al_2O_3} = 0.03$	$\phi_{Al_2O_3} = 0.04$	
3	0.70204642	0.719531478	0.737435414	0.7557736	1.79085
3.7	0.718533752	0.788333074	0.889210514	1.015145323	9.90712
4.9	0.780370295	0.931753125	1.122969268	1.342003469	18.76115
5.7	0.855189646	1.043874203	1.245861103	1.458150886	20.1087

Figs. 8.6 and 8.7, respectively. An increment in M retards both the velocity profiles. Physically, an augmentation in M enhances the Lorentz force (a conflicting force) that brings down the velocity. In addition, Lorentz force fuels a frictional force that leads to an escalation in the nanofluid temperature. Hence, $\theta(\zeta)$ increases with M (shown in Fig 8.8). The magnetic field parameter has a mixed impact on the nanofluid concentration (see Fig 8.9). Initially, $\phi(\zeta)$ decreases with M and gradually

Table 8.7: *Numerical estimation of Nu_r for various shapes of nanoparticles ($M = 0.2$, $Sc = 5$, $Nb = 0.2$, $Nt = 0.1$, $b_1 = 0.25$, $\gamma = 0.25$, $\zeta_\infty = 30$, $\tilde{N} = 100$.*

$\widetilde{n}_s$	Nu_r				Slope of $Nu_r = f(\widetilde{n}_s, \phi_{Al_2O_3})$
	$\phi_{Al_2O_3} = 0.01$	$\phi_{Al_2O_3} = 0.02$	$\phi_{Al_2O_3} = 0.03$	$\phi_{Al_2O_3} = 0.04$	
3	0.761567002	0.77656073	0.791540424	0.806513545	1.49819
3.7	0.763692739	0.778935228	0.791999253	0.802907625	1.30708
4.9	0.765231559	0.779448063	0.78971431	0.797404207	1.06784
5.7	0.763684413	0.777463582	0.789397437	0.800430499	1.22172

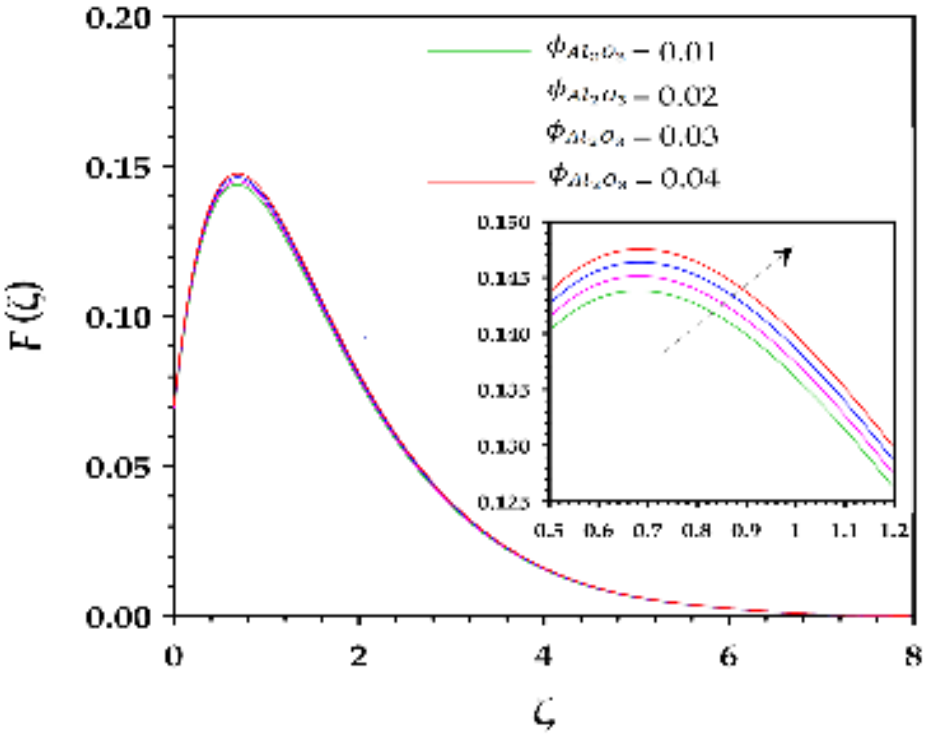

Figure 8.3: *Impact of $\phi_{Al_2O_3}$ on $F(\zeta)$.*

the trend reverses.

Figs. 8.10 and 8.11 depicts the consequence of b_1 on $F(\zeta)$ and $G(\zeta)$, respectively. An augmentation in b_1 transfers the stretching effects onto the fluid layers in the radial and azimuthal direction that decelerates the fluid flow. The positive impact of b_1 on the $\theta(\zeta)$ and $\phi(\zeta)$ has been illustrated in Figs. 8.12 and 8.13, respectively.

Fig. 8.14 elucidates the drop in $\theta(\zeta)$ due to escalating γ values. This is physically associated to the fact that mounting values of γ decreases the reactivity of fluid flow within the boundary layer, which reduces the amount of heat processed and thus

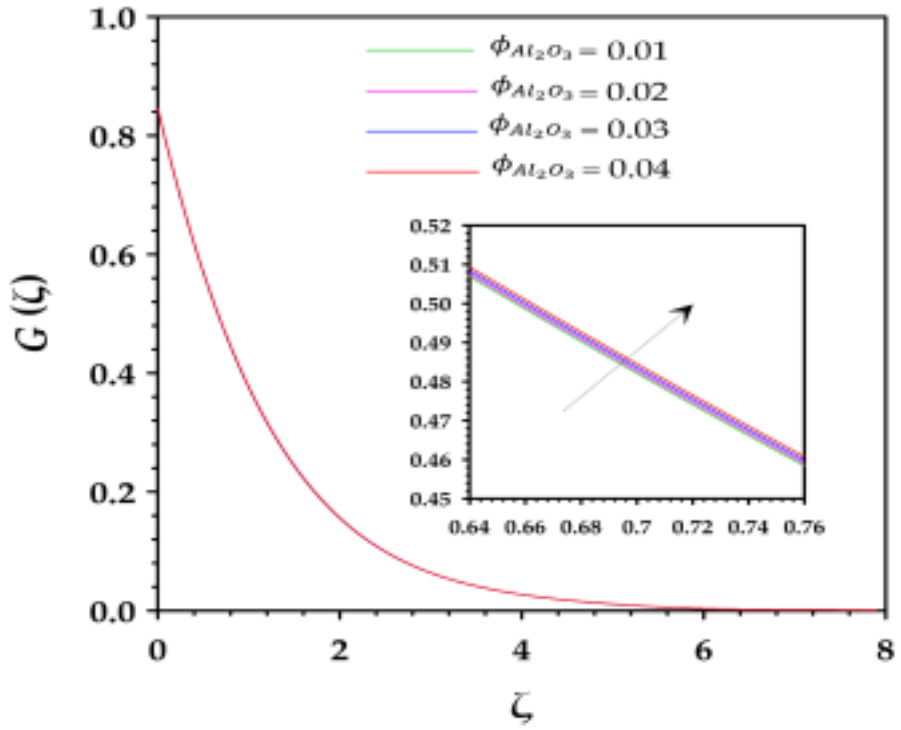

Figure 8.4: *Impact of* $\phi_{Al_2O_3}$ *on* $G(\zeta)$.

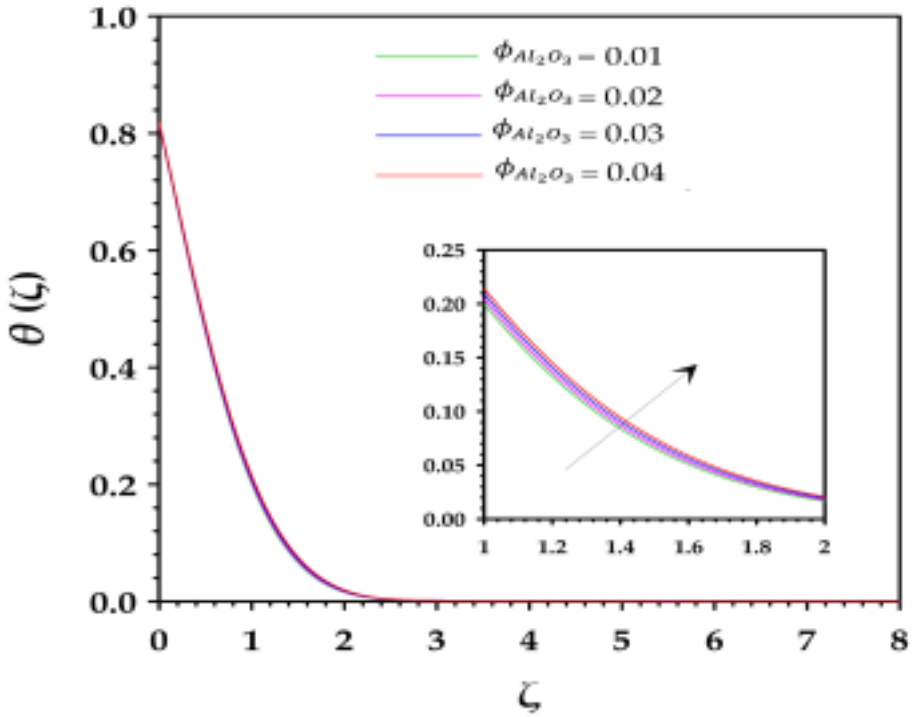

Figure 8.5: *Impact of* $\phi_{Al_2O_3}$ *on* $\theta(\zeta)$.

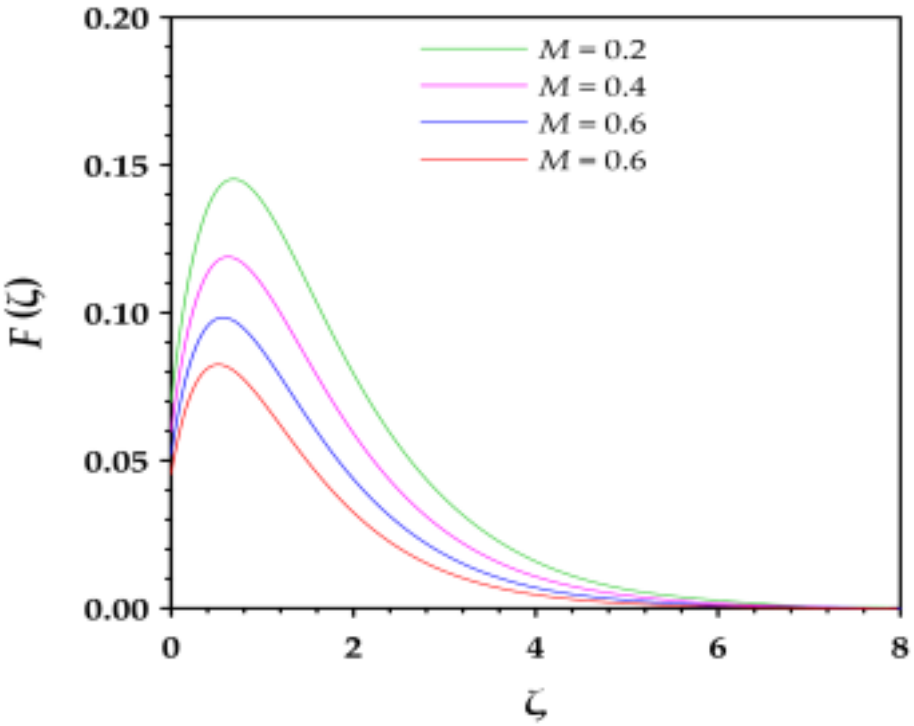

Figure 8.6: *Impact of* M *on* $F(\zeta)$.

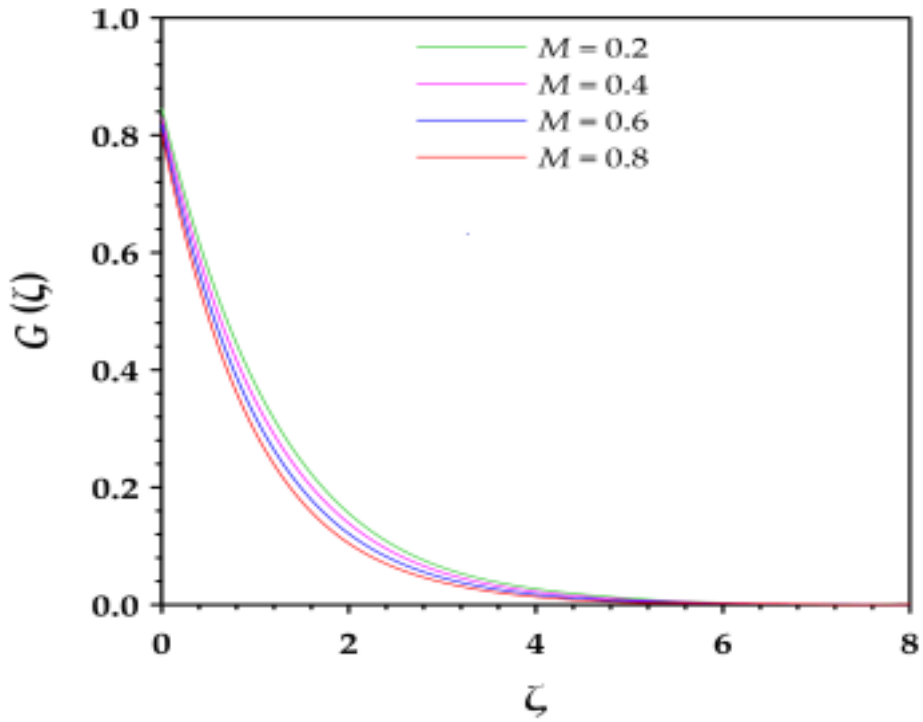

Figure 8.7: *Impact of* M *on* $G(\zeta)$.

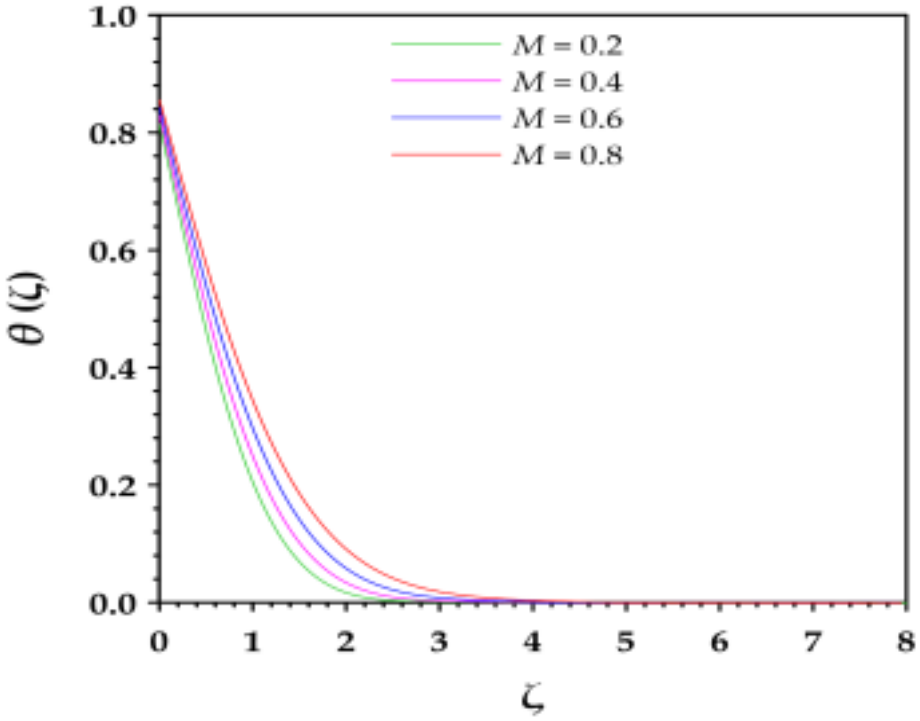

Figure 8.8: *Impact of* M *on* $\theta(\zeta)$.

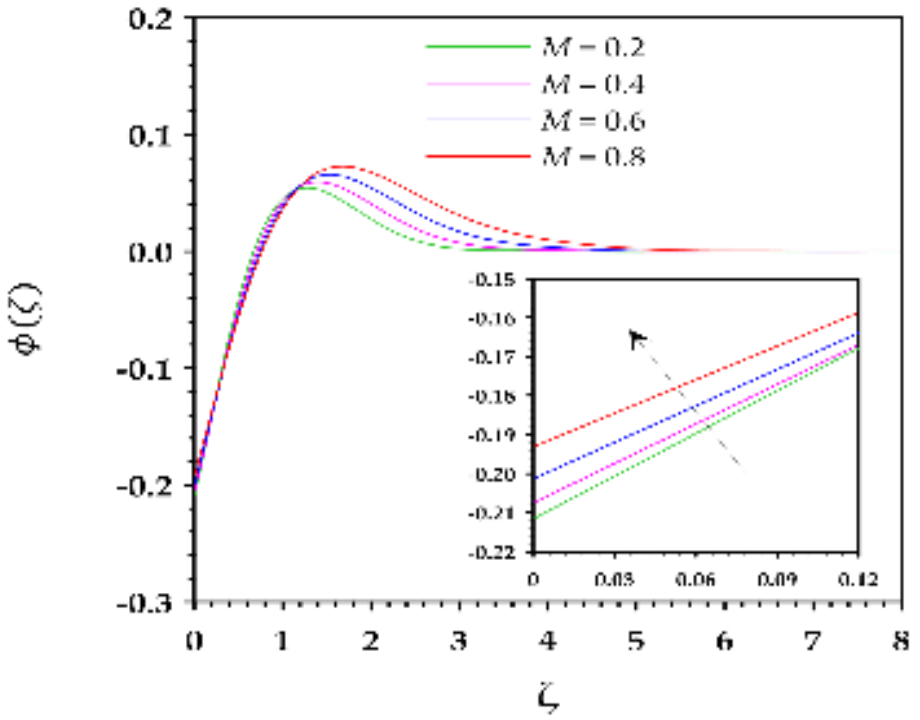

Figure 8.9: *Impact of* M *on* $\phi(\zeta)$.

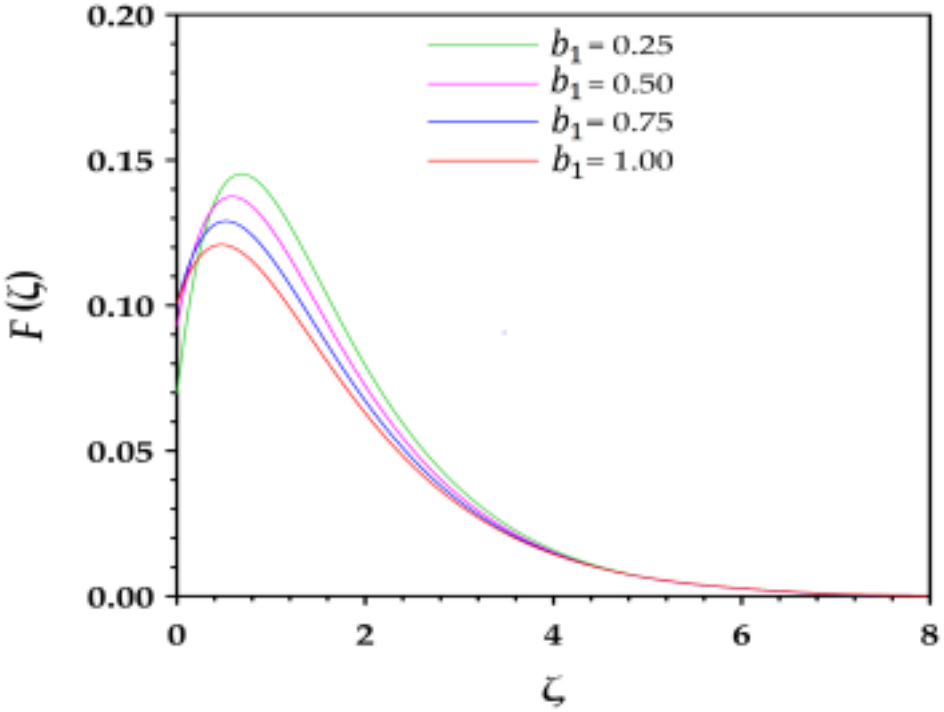

Figure 8.10: *Impact of* b_1 *on* $F(\zeta)$.

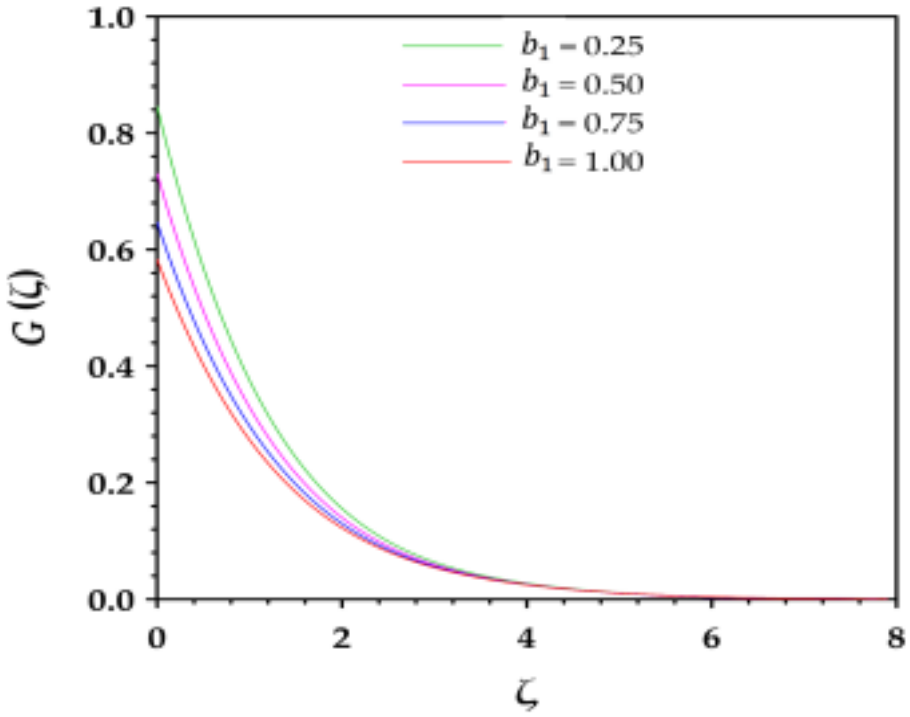

Figure 8.11: *Impact of* b_1 *on* $G(\zeta)$.

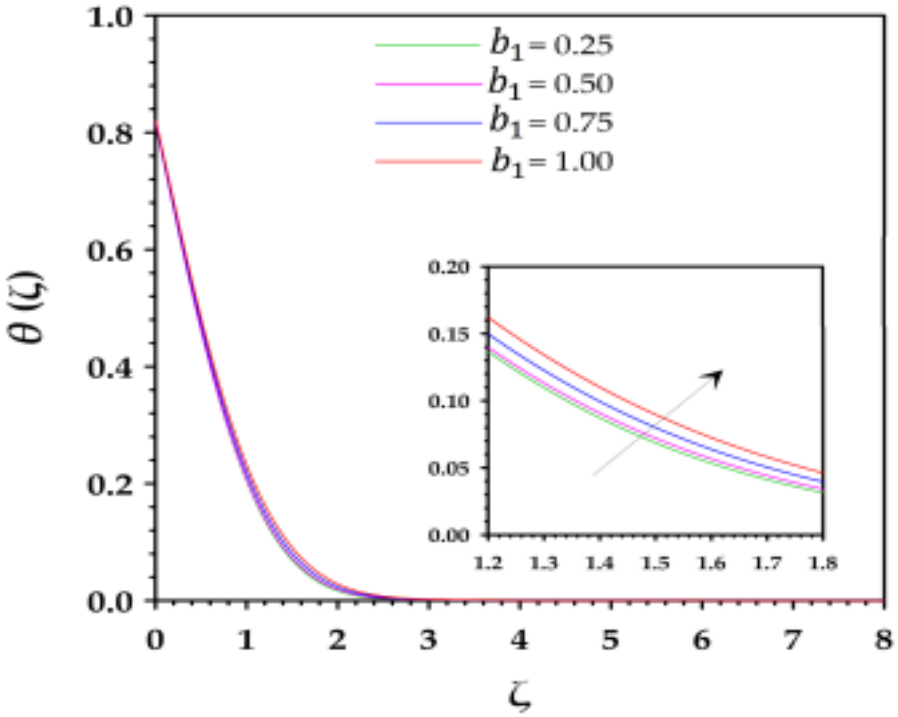

Figure 8.12: *Impact of* b_1 *on* $\theta(\zeta)$.

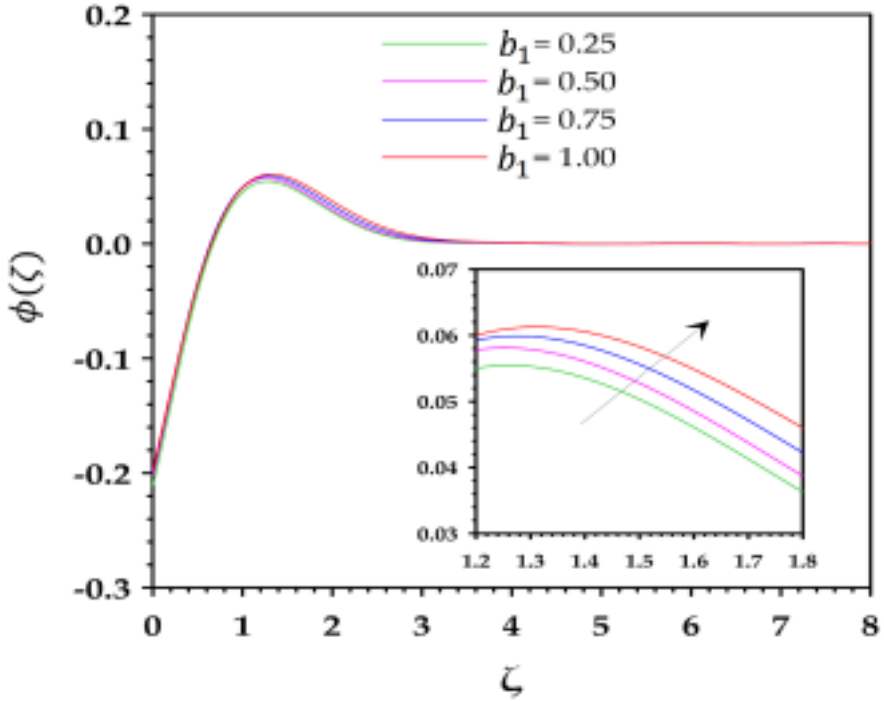

Figure 8.13: *Impact of* b_1 *on* $\phi(\zeta)$.

descends the nanofluid temperature. In addition, $\phi(\zeta)$ enhances near the disk and $\phi(\zeta)$ depletes away from the disk for augmenting values of γ (see Fig. 8.15). The flow rate is maximal away from the disk relative to the boundary layer which is the reason behind the decrease in nanofluid concentration.

The effect of Nt on $\theta(\zeta)$ and $\phi(\zeta)$ profiles are displayed in Figs. 8.16 and 8.17,

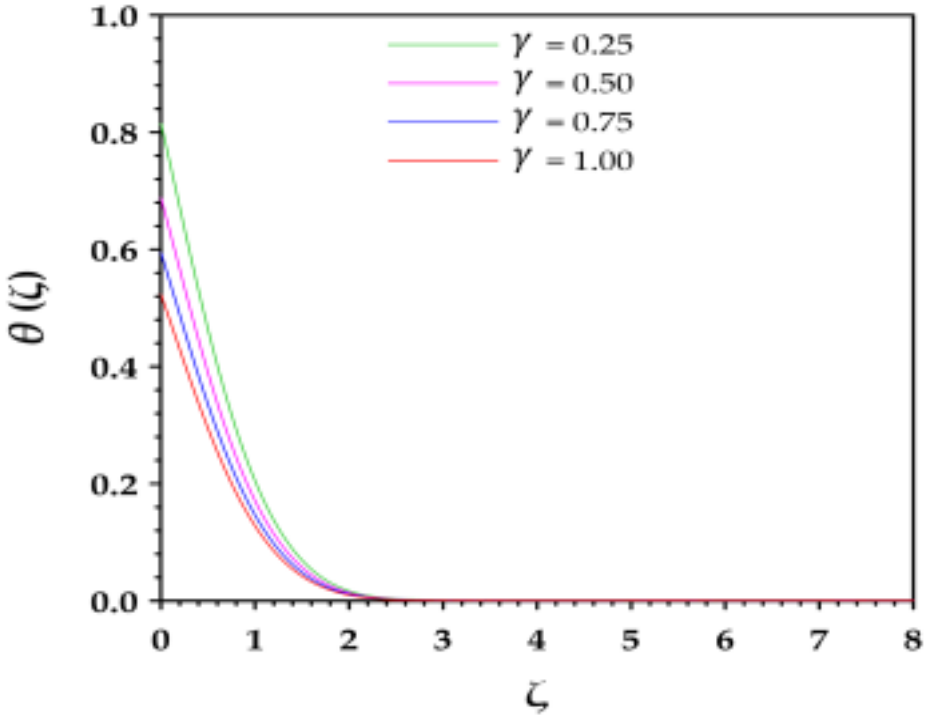

Figure 8.14: *Impact of* γ *on* $\theta(\zeta)$.

respectively. $\theta(\zeta)$ escalates with mounting Nt values and $\phi(\zeta)$ exhibits a negative impact near the disk which gradually transits into a positive impact (away from the disk). A rise in Nt accelerates the movement of hot fluid particles to the cold regions which enhances the thermal gradient and therefore the nanofluid temperature increases. Further, the increase in the nanofluid concentration away from the disk is due to improved mass transport caused by the movement of fluid particles from the disk to the ambient region.

Fig 8.18 elucidates the mixed impact of Nb on $\phi(\zeta)$. $\phi(\zeta)$ demotes near the disk and enhances away from the disk. Physically, an increment in Nb promotes the haphazard motion of nanoparticles that leads to increased collision near the disk (relative to away from the disk) caused by a large centrifugal force.

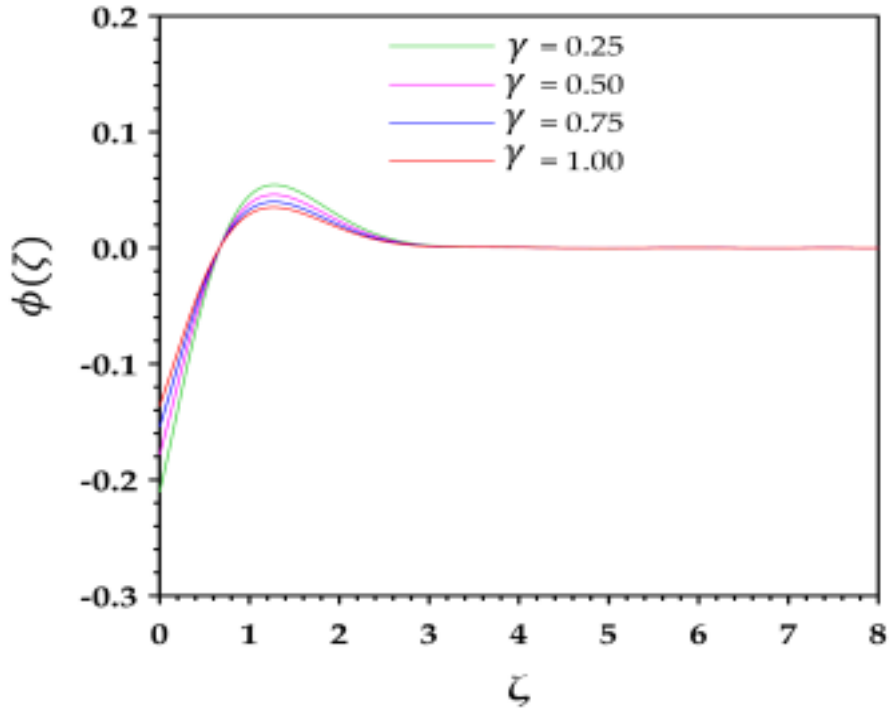

Figure 8.15: *Impact of* γ *on* $\phi(\zeta)$.

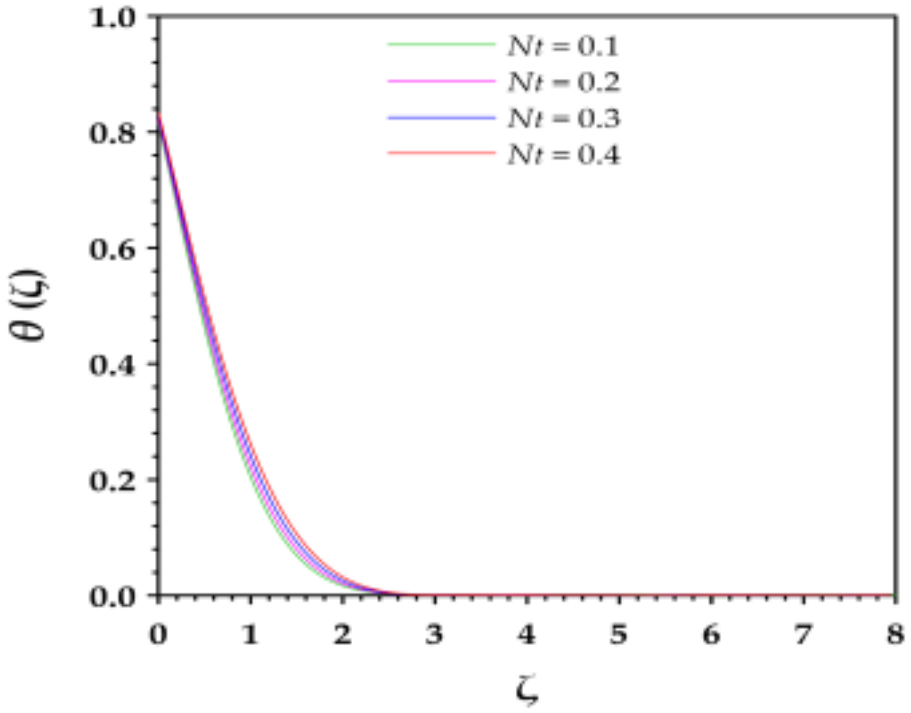

Figure 8.16: *Impact of* Nt *on* $\theta(\zeta)$.

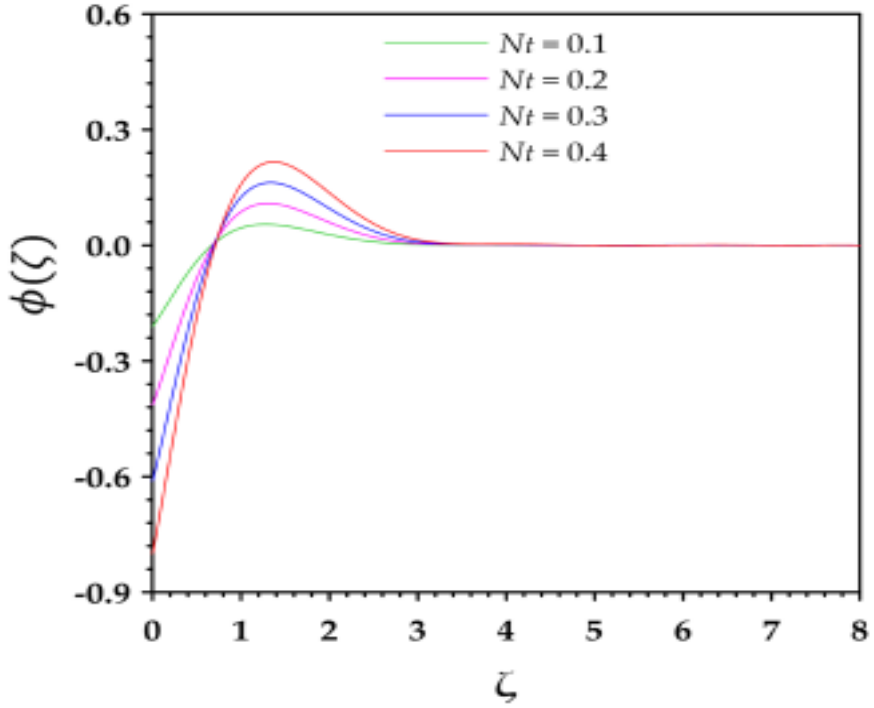

Figure 8.17: *Impact of* Nt *on* $\phi(\zeta)$.

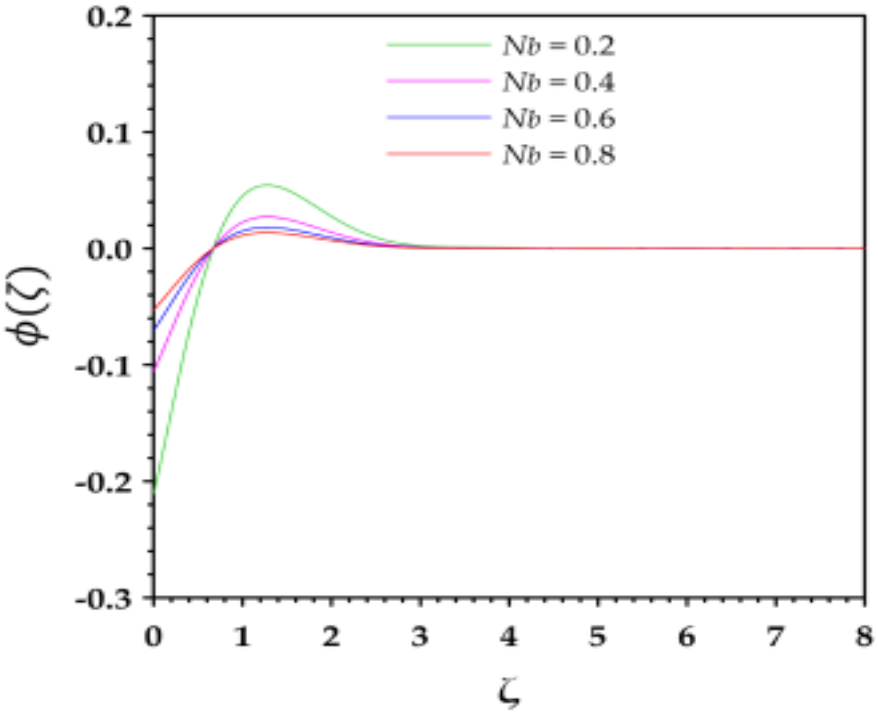

Figure 8.18: *Impact of* Nb *on* $\phi(\zeta)$.

Fig 8.19 depicts the influence of Sc on $\phi(\zeta)$. $\phi(\zeta)$ reduces near the disk and increases far from the disk. This is due to a mild diffusivity that encourages the nanoparticle migration from the hot disk towards the cold ambient fluid.

Figs. 8.20-8.23 illustrates significance of nanoparticle shape factor on $F(\zeta)$,

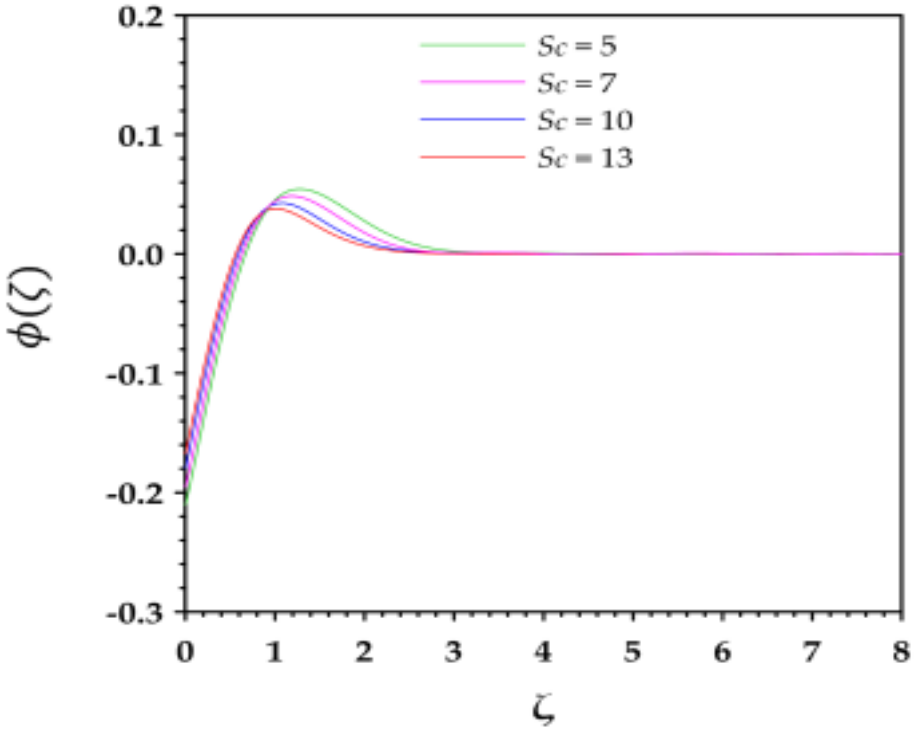

Figure 8.19: *Impact of Sc on $\phi(\zeta)$.*

$G(\zeta)$, $\theta(\zeta)$, and $\phi(\zeta)$, respectively. Initially, $F(\zeta)$ retards near the disk and gradually reverses the trend. In addition, $G(\zeta)$ and $\theta(\zeta)$ are increasing functions in $\widetilde{n_s}$ whereas $\phi(\zeta)$ is a reducing function of $\widetilde{n_s}$. Sphericity explores the resemblance of an object with a perfect sphere and the nanoparticle shape factor is inversely proportional to sphericity. An increment in the nanoparticle shape factor elevates the fluid flow in azimuthal direction due to the rotational effect. Further, augmenting $\widetilde{n_s}$ values exert more friction in the radial direction (near the disk) that helps in enhancing the nanofluid temperature. Tables 8.6 and 8.7 describe the influence of nanoparticle shape on the drag coefficient and the heat transfer rate, respectively. The highest drag is exhibited by platelet-shaped alumina nanoparticles followed by cylinder-, brick-, and sphere-shaped alumina nanoparticles. From Table 8.7, it can be concluded that heat transfer rate ascends with an increase in $\phi_{Al_2O_3}$.

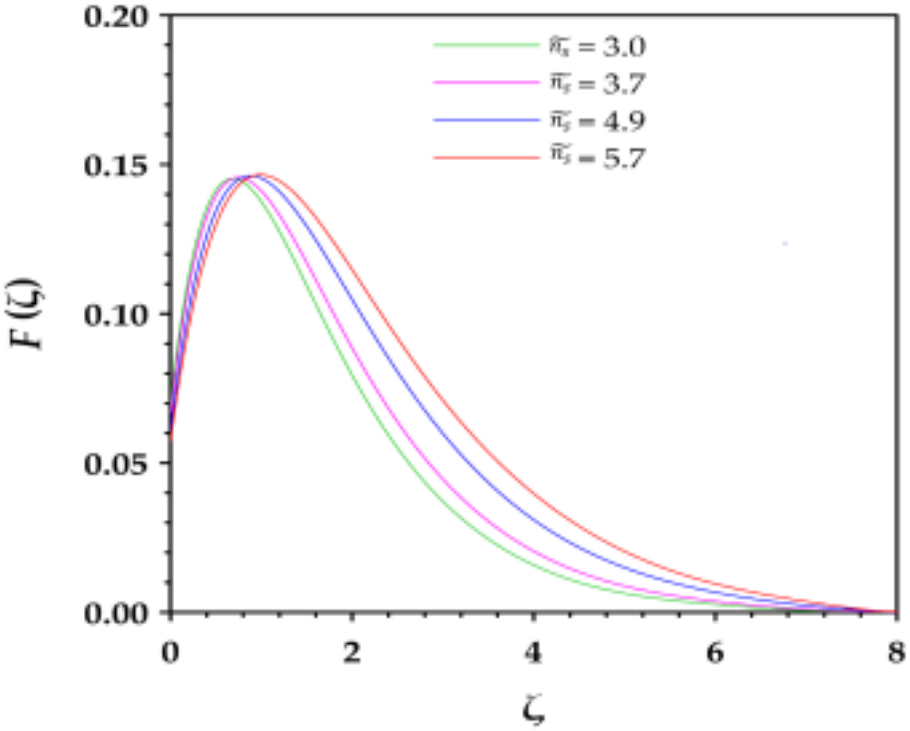

Figure 8.20: *Impact of* $\widetilde{n_s}$ *on* $F(\zeta)$.

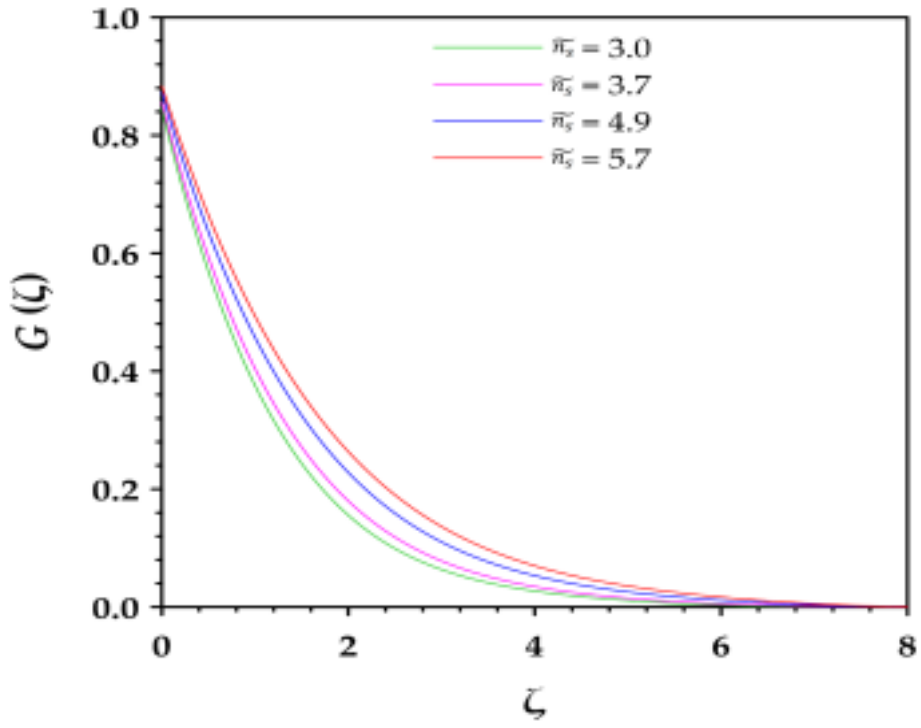

Figure 8.21: *Impact of* $\widetilde{n_s}$ *on* $G(\zeta)$.

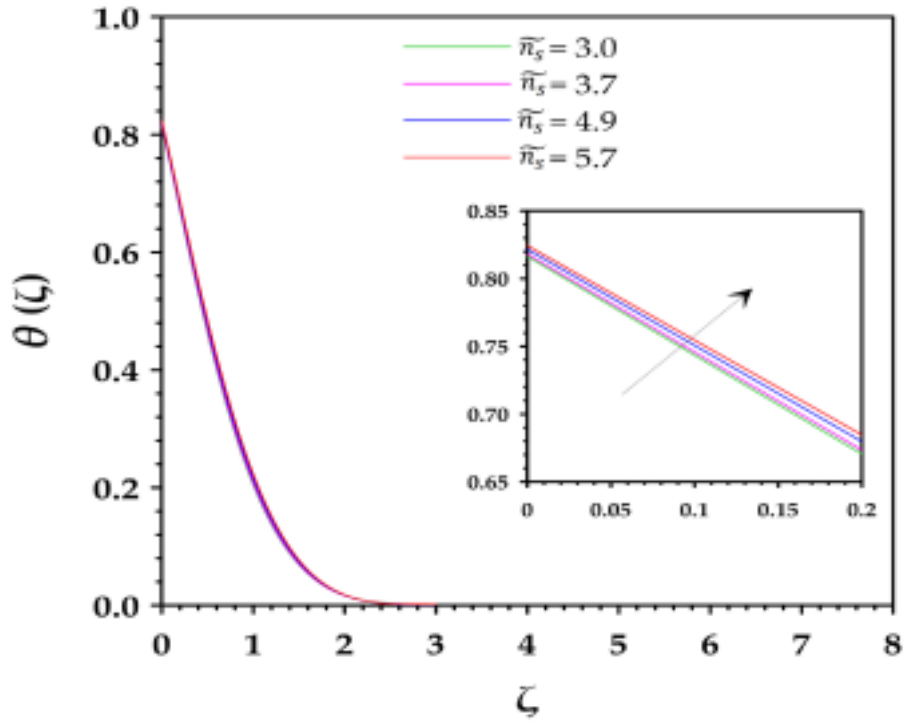

Figure 8.22: *Impact of* $\widetilde{n}_s$ *on* $\theta(\zeta)$.

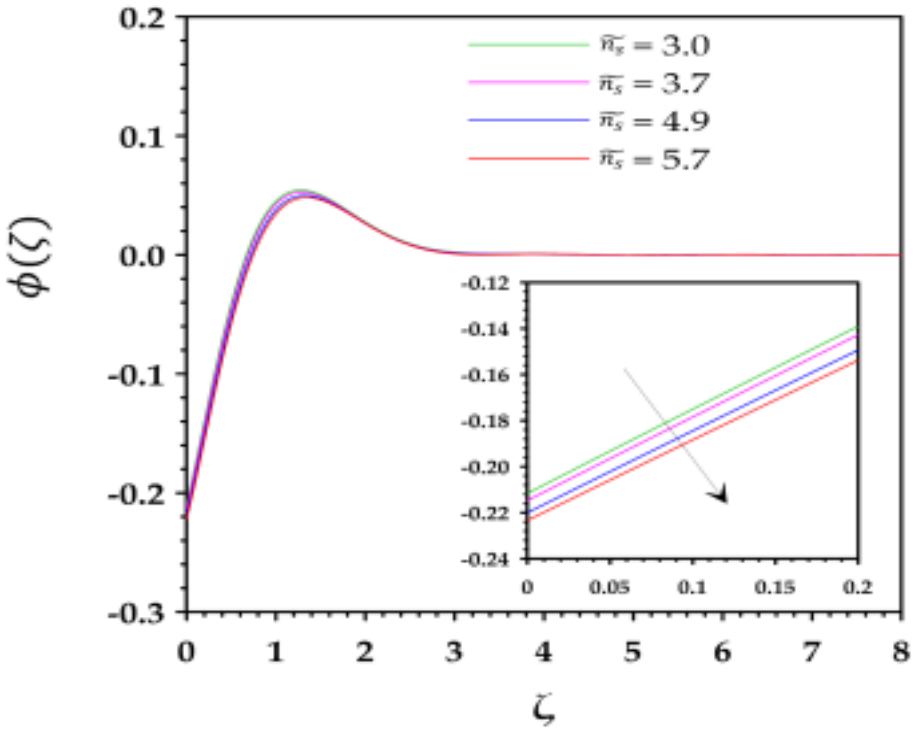

Figure 8.23: *Impact of* $\widetilde{n}_s$ *on* $\phi(\zeta)$.

8.5 Conclusions

The hydromagnetic alumina-water nanofluid flow past a rotating rigid disk has been theoretically investigated. The nanofluid flow considering different nanoparticle shapes (namely sphere, platelet, cylinder, and brick) and the thermo-hydrodynamic slip constraints have been modeled utilizing the modified Buongiorno model. The mathematically modeled equations are transmuted into a system of first-order ODEs using Von Kármán's similarity transformations and then resolved numerically by employing generalized differential quadrature method. The key conclusions of the present study are:

- The azimuthal velocity is inversely proportional to the hydrodynamic slip parameter.
- The nanofluid temperature ascends with the hydrodynamic slip parameter and descends with the thermal slip parameter.
- The nanofluid temperature is an increasing function of nanoparticle shape factor whereas the nanofluid concentration is a reducing function of nanoparticle shape factor.
- The heat transfer rate ascends with an increase in the volume fraction of alumina nanoparticle.
- The highest drag is exhibited by platelet-shaped alumina nanoparticles followed by cylinder-, brick-, and sphere-shaped alumina nanoparticles.